Author(s): Ylikorpi, Tomi & Forsman, Pekka & Halme, Aarne

Title: Dynamic Obstacle Overcoming Capability of Pendulum-driven Ball-Shaped Robots

Year: 2014

Version: Post print

Please cite the original version:

Ylikorpi, Tomi & Forsman, Pekka & Halme, Aarne. 2014. Dynamic Obstacle Overcoming Capability of Pendulum-driven Ball-Shaped Robots. 17th IASTED International Conference Robotics Applications (RA 2014). P. 329-338. ISBN 978-0-88986-968-4 (electronic).

DYNAMIC OBSTACLE OVERCOMING CAPABILITY OF PENDULUM-DRIVEN BALL-SHAPED ROBOTS

Tomi J. Ylikorpi, Pekka J. Forsman, Aarne J. Halme
Aalto University School of Electrical Engineering
Otaniementie 17, Espoo, Finland
Tomi.Ylikorpi@aalto.fi, Pekka.Forsman@aalto.fi, Aarne.Halme@aalto.fi

ABSTRACT
This paper discusses dynamic step-crossing capability of pendulum-driven ball-shaped robots. We introduce an extended dynamic model that allows modeling of ball-robot rolling, bouncing and slipping. Based on the new model, our simulations predict the maximum over-passable step-height for the robot. The simulation results agree well with the result from a parallel simulation in Adams-software as well as with practical experiments. The new dynamic model can be applied for mobility analysis of robot-ball designs as well as for path planning.

KEY WORDS
Ball-shaped robots, robot dynamics, robot kinematics, Euler-Lagrange equation, simulation.

NOMENCLATURE
The symbols are introduced in order of appearance. Units and hardware properties are added in parentheses (unit, GimBall, ShellBall). The Related work –section applies the notation of the original works as explained separately.

M_1	ball mass (kg, 3.39, 1.095)	M_2	pendulum mass (kg, 2.0, -)
R	ball radius (m, 0.226, 0.126)	e	pendulum length (m, 0.0787, -)
J_1	ball inertia (kgm^2, 0.0778, 0.011)	J_2	pendulum inertia (kgm^2, 0.0120, -)
θ_1	ball angle wrt. plane normal	θ_2	pendulum angle wrt. ball
T_1	ball kinetic energy	T_2	pendulum kinetic energy
V_1	ball potential energy	V_2	pendulum potential energy
τ,τ_1	motor torque on ball	τ,τ_2	motor torque on pendulum
v	ball velocity	v_{slip}	slip velocity
v_x	horizontal ball velocity	v_y	vertical ball velocity
x	horizontal ball location	y	vertical ball location
f_N	contact normal force	f_μ	contact friction force
μ	contact friction coefficient (plane, 0.22, 0.146) (step, 0.144, 0.12)	τ_μ	contact friction torque
		g	gravitational acceleration (m/s^2, 9.81)
$c1$	rolling friction (Nm, 0.005, 0.005)	$c2$	pendulum joint friction (Nm, 0.124, -)
k	shell contact stiffness (N/m, 33000, 67000)	kd	shell contact damping (Ns/m, 52, 50)
α	slope angle	h	step height
$\boldsymbol{d}$	contact vector	$\hat{\boldsymbol{d}}$	unit contact vector
$\hat{\boldsymbol{td}}$	unit normal vector for $\boldsymbol{d}$	kP	proportional gain
kD	derivative gain	kI	integral gain

μ_scale scaling factor for μ in modified Coulomb friction model
setangle target pendulum angle wrt. ground vertical
setvelocity target pendulum velocity wrt. ball velocity

1 Introduction

Ball-shaped vehicles have been under development already over the last 120 years. The first patents on self-propelled spherical toys were filed in the end of 19th century. Studies on dynamic modeling and steering of a motor-driven ball started in 1990's leading into emergence of computer controlled spherical mobile robots that recently have been introduced to commercial markets [1] - [7]. A spherical robot reaches its best mobility along smooth and level surfaces. Many of the applications relate to interaction with people in structured surroundings. Thus, typical applications for spherical robots frequently consider mobility in industrial plants, airports, and homes [5] - [7].

The motivation behind this paper anticipates a domestic rolling robot providing surveillance and companionship at home. Equipped with cameras, communications infrastructure and sensors; the robot moves autonomously monitoring the status and health of the environment and its inhabitants. The robot may join the human activities as a mobile messenger or as an interactive toy.

While the structured environment usually provides a beneficial rolling surface for a ball robot, also some usual every-day features create very probable obstacles for the robot. In home environment, such regular elements as door steps, carpets, vacuum cleaner electric cord, or scattered toys may form a notable obstruction for ball-robot mobility.

In order to design a spherical robot to surpass the predictable usual obstacles, there exists a need to estimate the step-overcoming capability of a ball-shaped robot. Further, this estimation is also needed for path-planning and controlling of robot motion in a structured environment.

Estimation of slope-climbing and step-crossing capability of ball-shaped robots has been customarily

conducted with a quasi-static analysis based on a static torque balance. With this approach, especially the step-crossing capability appears to be very limited being only some percents of the ball diameter [3], [4], [8] - [10]. Although some authors have noticed that dynamic behavior of the ball could help in passing over large obstacles, no attempts to calculate the dynamic obstacle overcoming capability of a motor-driven ball-robot have been presented.

In order to find out the dynamic operational performance of a ball-shaped robot, this paper introduces a method to predict the step-overcoming capability of a pendulum-driven spherical robot. We verify the results with dynamic simulations in two different simulators as well as with practical experiments

2 Related work

Plenty of prior work has been conducted on kinematic and dynamic modeling, path planning, and control of ball-shaped robots. The dynamic model of the robot relates closely to the applied mechanical structure and propulsion method. A motor-actuated hanging pendulum creates one possible driving mechanism [3], [5], [9]-[12]. There exists two popular methods to present the equations of motion of a pendulum-driven robot; A *coupled model,* presents the full motion of the complete system [13]–[18], while a *decoupled model* discusses the steering and forward-driving motions separately [3], [19]-[28]. A review on the forward-driving decoupled models is available in [29]. This paper continues the work initiated in context of [29] and applies the decoupled forward-motion model.

2.1 Mobility of internally propelled robots

Literature presents some papers discussing the motion of a pendulum-driven ball-robot on a sloped surface and/or the ability of the ball to overcome obstacles. Fig. 1 presents an illustration of a typical pendulum-driven ball.

In analysis of ball mobility, Koshiyama and Yamafuji include the slope angle in the dynamic equations [3]. Simulation of the decoupled robot model shows the ball ascending a 0.1-rad slope. No attention is paid for the necessary contact friction or maximum traversable slope.

Halme et al. calculate the mass-center of the complete ball-robot, including the spherical shell and the *inside driving unit (IDU)* [4]. For overcoming a step-shaped obstacle, they calculate the quasi-static torque balance about the contact point at the corner of the step. The result is expressed with the two separate masses: one for the IDU and one for the spherical shell:

$$h_{max} = R_1 - \sqrt{R_1^2 - \left(\frac{mr}{M_{ball}+m}\right)^2}, \qquad (1)$$

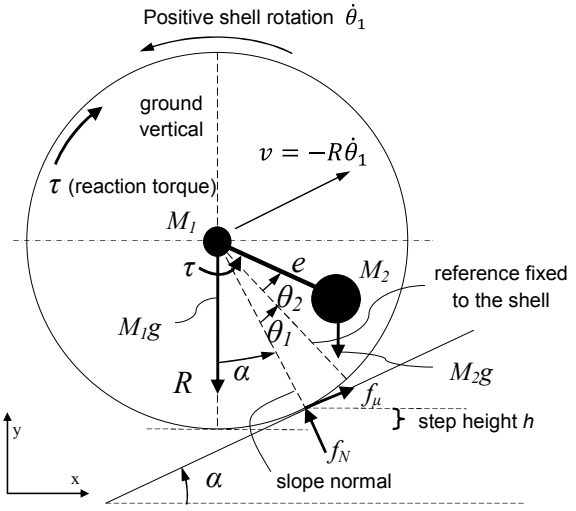

Fig. 1. Typical decoupled model of a pendulum-driven ball-robot ascending a slope, or a step with height *h*.

where: h = step height, R_1 = ball radius, r = IDU mass-center off-set, m = IDU mass, M_{ball} = spherical shell mass.

While (1) presents the maximum obstacle height for a quasi-static balance, Halme et al. note that any initial rolling velocity of the robot would help to overcome an obstacle also larger than the result implies. A few additional papers reach an identical result [8] - [10]. They all notify the significantly small step height, being only 0.5-2% of the ball radius. They also assume sufficient contact friction and ignore any dynamic effects.

In addition to no-slip-assumption, Laplante calculates also the contact force between the ball and the slope [10]. Knowledge of the normal force and the coefficient of friction allows calculation of the maximum traversable slope where slipping will not happen. Laplante notices that for his ball-robot, assuming a contact coefficient of friction 0.2, the maximum theoretical traversable slope angle is as much as 48 degrees. However, the robot mass distribution limits the mechanical slope climbing capability to gentle 7.68 degrees.

Yu et al. introduce another spherical mobile robot *BYQ-III* with a pendulum-based propulsion mechanism [15]. Using body-fixed ZYX-Euler rotations, they present 3D-rolling kinematics of the spherical shell. Dynamic equations of motion are derived using the Euler-Lagrange equation with constraints. Simulations demonstrate the model behavior on an inclined slope as well as on a 3D-surface. The significant effect of the surface geometry on the robot trajectory is notified. The model assumes no-slip condition and neglects the consideration of maximum available driving torque or contact friction.

In another paper, Yu et al. present the spherical mobile robot *BYQ-VIII,* as well equipped with a driving pendulum [27]. The dynamic model acquired with Euler-Lagrange equation limits on 2D-motion along a slope. Yu et al. find

the equilibrium state on the slope by setting the angular acceleration and velocity zero. They continue the analysis in 3D but limit the 3D-surface as a sloped plane.

Zhao et al. introduce a model of a spherical mobile robot on the Moon surface [30]. The model presents contact geometry, contact pressure and rolling friction between a rolling sphere and Lunar soil. The soil resistance against ball motion constitutes components of soil normal stress and shear stress. Slopes, obstacles or maximum driving torque of the robot are not included in the model.

2.2 Mobility of wind driven robots

Wind-driven balls present another branch of spherical vehicles whose mobility has been explored in detail. Based on the concept presented by Jacques Blamont, *Tumbleweed* is a spherical wind-propelled robot designed to travel on the surface of Mars [31].

Plenty of prior work exists on aerodynamic modeling, motion modeling, and simulations of wind-driven Martian rovers. Based on the wind velocity, drag coefficient, and the ball projection area, Antol et al. calculate the lateral thrust force on a wind-driven Tumbleweed-robot [31]. Quasi-static torque balance against the corner of a step-shaped obstacle then reveals the maximum possible step height to be passed.

$$h_{max} = r\left(1 - \sqrt{\frac{(mg_{mars})^2}{\left[C_D\pi r^2\left(\frac{1}{2}\rho V_{nom}^2\right)\right]^2 + (mg_{mars})^2}}\right), \quad (2)$$

where: r = Tumbleweed radius, m = Tumbleweed mass, g_{mars} = gravity on Mars, C_D = drag coefficient, ρ = atmospheric density, V_{nom} = nominal wind velocity.

Kolacinski and Quinn consider both quasi-static and dynamic effects in obstacle overcoming [32]. Their energy-based model assumes the preservation of energy and describes the maximum obstacle height as a function of the initial velocity. Considering the coefficient of restitution and Coulomb friction, another model was created in dynamics simulation software to model impacts. Comparison of the simulation results show that the quasi-static model, when compared to the dynamic simulation, under-estimates the ball mobility while the energy-based model over-estimates it.

Flick and Toniolo apply the quasi-static torque balance to study Tumbleweed mobility if trapped between obstacles on a slope [33]. They present simulation results of Tumbleweed colliding with a step-shaped obstacle and being pushed by a Martian wind when air-borne. To relate the ball velocities before and after the impact, the collision model applies the restitution coefficient.

Hartl simulates numerically the motion of a Tumbleweed rover as it encounters ravines and valleys on Martian surface [34]. Based on the collision model of Kane and Levinson [35], the simulator covers rolling, sliding and bouncing behaviors of the rover, as well as the transitions between these motion modes. Hartl notifies the minimum value of the coefficient of static friction compatible with rolling on the inclined plane.

Using Kane's method and Newton mechanics, Li and Liu apply a similar methodology as Hartl in describing the ball rolling, slipping and bouncing [36]. To propel the robot forward, Li and Liu add a thrust force presented by a stochastic wind model. To pass large obstacles, their model utilizes increased buoyancy achieved by a volumetric expansion of the sphere.

As well for wind-propelled planetary exploration, Liang et al. introduce a deformable spherical robot constructed of a wire frame and airbags attached to each wire. The airbags, when inflated, complete the wire frame into a full sphere [37]. For analytical mobility estimation, Liang et al. consider the wind pressure and rolling friction on a rolling sphere so to reach an estimate for the ball velocity. According to the simulations in Adams-simulation software, the 1-m spherical robot can climb terrestrial 30-degree slopes and cross 0.25-m obstacles, when the wind speed is 8m/s.

3 Equations of motion

Previous work has considered the mobility of motor-driven ball-robots through quasistatic torque balance neglecting dynamic effects. The dynamic analysis of a wind-driven Tumbleweed-ball has been divided in two phases: The bouncing contacts have been modeled as incidents considering the restitution coefficient and preservation of momentum, while the rolling and flying between the impacts is modeled with second-order differential equations.

The current state of the art does not present any dynamic analysis for a pendulum-driven robot encountering obstacles. In the following, we introduce dynamic equations that describe the motion of a pendulum-driven ball-robot when rolling or bouncing, and also during a contact. This model can be used to analyze the ball behavior upon contacts with obstacles. The dynamic model is the same for all phases of the ball motion, only the contact force function changes according to the prevailing contact condition.

3.1 Derivation of the equations of motion

Euler-Lagrange equation is often used to create the equations of motion [38], [39], which has been demonstrated with ball-shaped robots for example in [19], [21] and [24]. The related work has been reviewed in [29] explaining also the application of the Euler-Lagrange equation for pendulum-driven robots.

In application of the Euler-Lagrange equation, so called

generalized coordinates are used to describe the ball state. With the generalized coordinates, the system energy and the *Lagrangian function* are derived as well. In previous works, the chosen generalized coordinates represent the rotation angles of the ball and the pendulum, indicated by θ_1 and θ_2 in Fig. 1. In addition, the ball motion is kinematically constrained to present rolling without slipping.

In our new model, we replace the rolling constraint with linear ball velocities and contact forces. The traditional generalized coordinates are then added with the horizontal and vertical position of the ball. The new generalized coordinates are:

$$\boldsymbol{q} = (\theta_1, \theta_2, x, y) \tag{3}$$

Kinetic and potential energy of the robot can be expressed with the new generalized coordinates as:

$$\begin{aligned} T_1 &= \tfrac{1}{2}J_1\dot{\theta}_1{}^2 + \tfrac{1}{2}M_1{v_x}^2 + \tfrac{1}{2}M_1{v_y}^2 \\ T_2 &= \tfrac{1}{2}M_2\left(\left(v_x + e\left(\dot{\theta}_1 + \dot{\theta}_2\right)cos(\alpha + \theta_1 + \theta_2)\right)^2\right) + \\ &\tfrac{1}{2}M_2\left(v_y + e\left(\dot{\theta}_1 + \dot{\theta}_2\right)sin(\alpha + \theta_1 + \theta_2)\right)^2 + \tfrac{1}{2}J_2\left(\dot{\theta}_1 + \dot{\theta}_2\right)^2 \end{aligned} \tag{4}$$

$$\begin{aligned} V_1 &= M_1 g y \\ V_2 &= M_2 g\left(y - ecos(\alpha + \theta_1 + \theta_2)\right) \end{aligned} \tag{5}$$

With application of the Euler-Lagrange equation, as described for example in [29], the dynamic equations of motion can be derived from (4) and (5). The result may be then presented in *configuration space* according to (6), where $\boldsymbol{A}$, $\boldsymbol{B}$, $\boldsymbol{C}$, $\boldsymbol{D}$ and $\boldsymbol{G}$ present the matrices including the mass and inertia terms, the centrifugal terms, the coriolis terms, viscous friction, and the gravitational forces respectively [3].

$$\boldsymbol{A}_{4x4}\begin{bmatrix}\ddot{\theta}_1\\ \ddot{\theta}_2\\ \ddot{x}\\ \ddot{y}\end{bmatrix} + \boldsymbol{B}_{4x4}\begin{bmatrix}\dot{\theta}_1^2\\ \dot{\theta}_2^2\\ \dot{x}^2\\ \dot{y}^2\end{bmatrix} + \boldsymbol{C}_{4x4}\begin{bmatrix}\dot{\theta}_1\dot{\theta}_2\\ \dot{\theta}_2\dot{x}\\ \dot{x}\dot{y}\\ \dot{x}\dot{\theta}_1\end{bmatrix} + \boldsymbol{D}_{4x4}\begin{bmatrix}\dot{\theta}_1\\ \dot{\theta}_2\\ \dot{x}\\ \dot{y}\end{bmatrix} + \boldsymbol{G}_{4x1} = \begin{bmatrix}\tau_1\\ \tau_2\\ F_x\\ F_y\end{bmatrix} \tag{6}$$

The matrix elements in (6) are explained below. Element *D11* presents the viscous rolling resistance on the ball, while *D22* presents the viscous joint friction between the ball and the pendulum arm.

$$\begin{aligned} &A11 = J_1 + J_2 + M_2e^2 \\ &A12, A21, A22 = J_2 + M_2e^2 \\ &A13, A23, A31, A32 = M_2ecos(\theta_1 + \theta_2) \\ &A14, A24, A41, A42 = M_2esin(\theta_1 + \theta_2) \\ &A33, A44 = M_1 + M_2 \\ &B31, B32 = -M_2e\sin(\theta_1 + \theta_2) \\ &B41, B42 = M_2e\cos(\theta_1 + \theta_2) \\ &C31 = -2M_2e\sin(\theta_1 + \theta_2) \\ &C41 = 2M_2e\cos(\theta_1 + \theta_2) \\ &D11 = c_1, D22 = c_2 \\ &G1, G2 = M_2ge\sin(\theta_1 + \theta_2) \\ &G4 = (M_1 + M_2)g \end{aligned}$$

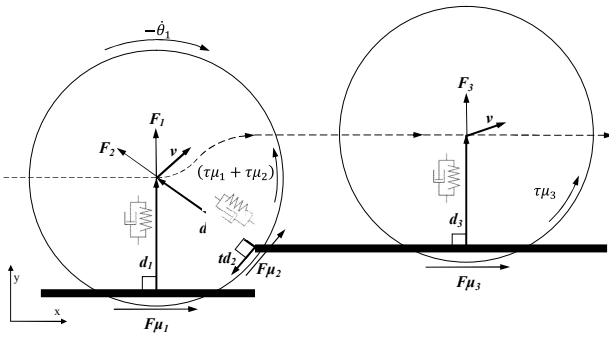

Fig. 2. Three contacts act on a ball rolling over a step-shaped obstacle. Normal forces act towards the ball center, tangential friction forces create friction torque

4 Generalized forces

To complete the dynamic model, the generalized forces on the right side of (6) must be calculated. These forces and torques originate from ball contacts with the environment, as well as from the pendulum motor torque.

4.1 Contact model

Contact model includes three separate contacts illustrated in Fig. 2. The figure shows the contact with the lower rolling plane, the contact with the corner of the step-shaped obstacle, and the contact with the upper rolling plane on top of the step.

Contact force is calculated using an *impact*-model where the contact constitutes a spring and a viscous damper. Spring ratio is set to be constant, i.e. the penetration depth exponent in force-function is 1. Viscous damping is equal for contact penetration and retraction. Adams-simulation software applies a similar contact model [40] - [43].

In Fig. 2, vectors $\boldsymbol{d_{1\text{-}3}}$ present the distance from the contacting surface to the ball center. Normal forces $F_{1\text{-}3}$ prevent the ball penetration through the surface. The spring force acting along the contact vectors $\boldsymbol{d_{1\text{-}3}}$ is directly proportional to the penetration depth. Additional viscous contact force develops from the penetration velocity. The normal contact force acting towards the ball center is then

$$\boldsymbol{F} = \left(k(R - |\boldsymbol{d}|) - kd\left(\boldsymbol{v}\cdot\widehat{\boldsymbol{d}}\right)\right)\widehat{\boldsymbol{d}} \tag{7}$$

Slip velocity vector $\boldsymbol{v_{slip}}$ describes ball slipping and sliding at the contact point and it affects the ball through contact friction. Slip velocity presents the velocity of a point on ball surface wrt. the stationary plane or the step corner as

$$\boldsymbol{v_{slip}} = \left(\boldsymbol{v} - R\dot{\theta}_1\widehat{\boldsymbol{td}}\right) \tag{8}$$

For contact friction force, a modified Coulomb friction model without stiction is applied. In the modified model, the friction force is continuous in vicinity of zero slip

velocity [44], [45]. Also Adams simulation software applies a variant of the modified Coulomb friction model [40] - [43]. We apply this model by scaling down the effective coefficient of friction in vicinity of zero slip velocity. In absence of slip, the effective coefficient of friction is zero but it reaches the nominal value at 0.01 m/s slip velocity as the scaling factor μ_scale reaches the value 1 in (9).

$$\boldsymbol{F_\mu} = -|\boldsymbol{F}| \cdot \mu \cdot \mu\_scale \cdot \hat{\boldsymbol{v}}_{\boldsymbol{slip}} \quad (9)$$

As this contact force affects on the surface of the ball, slipping also creates a torque around the ball center

$$\boldsymbol{\tau_\mu} = \boldsymbol{F_\mu} \times \boldsymbol{d} \quad (10)$$

Once the forces $\boldsymbol{F}$ and $\boldsymbol{F_\mu}$, and the torque $\boldsymbol{\tau_\mu}$ have been derived and divided into horizontal and vertical components, they can be placed on the right side of (6) to present the generalized forces F_x, F_y and τ_1.

4.2 Pendulum driving torque

The pendulum driving torque τ_2 on the right side of (6) depends on the pendulum actuation. The simulations performed for this paper consider three different cases in which the pendulum is either a) completely free, b) under position control, or c) under velocity control.

a) A freely rolling case avoids the necessity to model accurately the electromechanical and dynamic properties of the driving motor or the control system. In simulator, the pendulum driving torque τ_2 is then set to zero. Respectively in the practical experiments, the pendulum motor is detached from the power transmission by removing the pinion from the motor shaft. The ball then freely rolls down a slope to reach the impact velocity.

b) In the second simulation case, a closed loop-controller was applied to maintain the desired pendulum angle. A PD-controller with gravity compensation was utilized with gains $kP = 40$ and $kD = 10$.

$$\tau_2 = kP \cdot \left(setangle - (\theta_1 + \theta_2)\right) - kD \cdot \left(\dot{\theta}_1 + \dot{\theta}_2\right) + M_2 gesin(\theta_1 + \theta_2) \quad (11)$$

In the simulation, the controller aims to maintain the desired pendulum angle during and after the collision. Three different cases are simulated: pendulum pointing downwards ($\theta_2 = 0$), pendulum elevated 90 degrees ($\theta_2 = \pi/2$), and pendulum pointing upwards ($\theta_2 = \pi$).

c) While a constant pendulum angle provides a constant acceleration for the ball, the ball-robot is often driven under velocity control. The third controller in the simulation mimics a velocity controller that keeps the pendulum rotation velocity wrt. the ball as constant. A P-controller with gravity compensation is applied. Proportional gain kP is 10 while the integrator was found unnecessary and kI remains zero.

$$\tau_2 = kP \cdot \left(setvelocity - \dot{\theta}_2\right) + kI \cdot (setvelocity \cdot t - \theta_2) + M_2 gesin(\theta_1 + \theta_2) \quad (12)$$

5 Numerical simulators

We have verified the model through simulations in Matlab-software of MathWorks Inc. (Version 7.5.0.342, R2007b). The dynamic model in configuration space, shown in (6), is used to solve the accelerations for the given input torque. To receive the joint velocities and angles, ode23t – solver function is then applied in integration of the accelerations. Table 1 presents the solver parameters for the simulator in Matlab as well as for the simulation in Adams multi-body simulation software of MSC.Software Corporation (Version MD Adams R3, Build 2008.1.0).

Table 1

MATLAB SOLVER PARAMETERS

Solver	ode23t
Output time step	0.1 s
RelTol	1E-6
AbsTol	1E-9
MaxStep	1E-3
InitialStep	1E-6

ADAMS SOLVER PARAMETERS

Solver	C++
Corrector	Original
Integrator	GSTIFF (Newton-Raphson)
Formulation	I3
Output time step	0.1 s
Units	m-kg-s
Error	1E-9
Hmax	1E-3
Hmin	1E-10
Hinit	1E-6
Adaptivity	off
Interpolate	off
Kmax	6
Maxit	10

5.1 Simulation in Matlab-software

Ball-simulator in Matlab-software takes as an input the initial conditions including ball velocity, pendulum angle, ball distance to the step, step height and the angle of the slope behind the step. The generalized forces are calculated with the aid of the contact model and pendulum motor actuation according to (7) - (12). The dynamic model (6) is then applied according to (13) to calculate the accelerations.

$$\begin{bmatrix}\ddot{\theta}_1\\ \ddot{\theta}_2\\ \ddot{x}\\ \ddot{y}\end{bmatrix} = \boldsymbol{A^{-1}}\left(\begin{bmatrix}\tau_1\\ \tau_2\\ F_x\\ F_y\end{bmatrix} - \boldsymbol{B}\begin{bmatrix}\dot{\theta}_1^2\\ \dot{\theta}_2^2\\ \dot{x}^2\\ \dot{y}^2\end{bmatrix} - \boldsymbol{C}\begin{bmatrix}\dot{\theta}_1\dot{\theta}_2\\ \dot{\theta}_2\dot{x}\\ \dot{x}\dot{y}\\ \dot{x}\dot{\theta}_1\end{bmatrix} - \boldsymbol{D}\begin{bmatrix}\dot{\theta}_1\\ \dot{\theta}_2\\ \dot{x}\\ \dot{y}\end{bmatrix} - \boldsymbol{G}\right) \quad (13)$$

For the given collision velocity, the maximum traversable step height can be found only by trial and error. An ascending bracketing method is used to search for the maximum step height for each given velocity. The step height iteration is repeated for all velocities that are desired to be studied.

5.2 Simulation in Adams-software

In addition to simulations in Matlab, a comparative simulation in Adams multi-body simulation software was performed for validation.

The ball robot model in Adams-environment is defined by the mechanical structure and the physical properties of the robot. Adams autonomously creates the dynamic model needed for simulations. Thus, Adams provides a dynamic model that is independent from the one we have created and simulated in Matlab. Therefore, the simulation results from Adams can be used for validation of our dynamic model. Fig. 3 illustrates the graphical result of one simulation run in Adams.

6 Experimental Tests

Experimental tests were performed for validation of the simulation models. In the tests, different balls were rolled down a sloped ramp to collide with a step-shaped obstacle. Collision velocity was varied and measured for each pre-set step height. The collision velocity, step height and observation whether the ball passed the step were recorded. Step height was gradually increased from 5 mm to 55 mm in ~5 mm steps.

Fig. 4 shows the test items together with the platform, the sloped ramp and the adjustable step. The first test item is the pendulum-driven *GimBall*-robot, 45 cm in diameter and weighing 5.4 kg. For free-rolling tests, the pendulum motor pinion has been removed. The second test item is called as *ShellBall*. The white 25-cm diameter ShellBall constitutes only a stiff 1.1-kg spherical shell, without any other components. System properties for the GimBall and ShellBall are visible in Nomenclature.

For ball velocity measurement, a data-acquisition unit reads at 1 kHz frequency two resistive touch sensors (not shown in the figure) placed 100 mm apart in front of the step. Measurement software checks the measured data, calculates ball velocity, and stores successful measurements on a file. Rolling tests for the given step height are repeated until the maximum no-pass velocity has been found. Then the step height is increased 5 mm

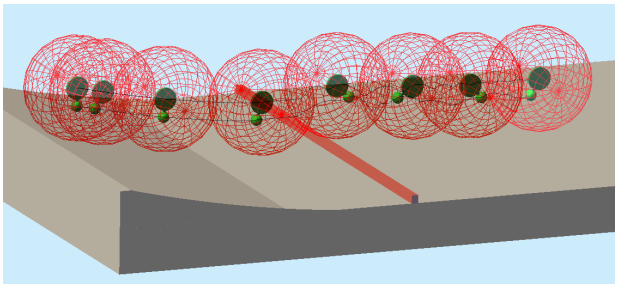

Fig. 3. Free rolling Simulation in Adams

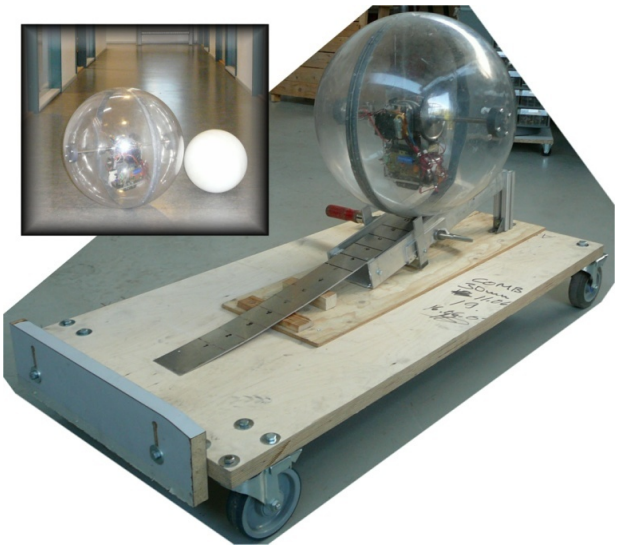

Fig. 4. Two spherical test items for the experimental tests (inset), the adjustable step-shaped obstacle and the slope

and the procedure repeats.

In addition to the free-rolling tests, also an active-driving test was performed with the GimBall. In this test, the slope was removed and the ball was driven with its internal motor, manually commanded with wireless radio-control equipment. The pendulum motor is driven in open-loop voltage control, without any other than visual feedback from the pendulum velocity and position. The platform length allowed a 120-cm long acceleration period before colliding with the step.

7 Simulations and experimental results

In the first tests and simulations the balls were rolling freely along an inclined slope and colliding with a step at a measured velocity. Fig. 5 shows the free-rolling simulation results of the dynamic model as well as the test results for the ShellBall (left) and GimBall (right). The simulation results agree well with the test results. Non-idealities in physical properties of the robot, as well as the varying pendulum orientation at the moment of impact, cause some divergence in the measured pass and no-pass velocities.

Fig. 6 presents GimBall step crossing performance under manual velocity control, compared to the simulated results with pendulum pointing downwards and with pendulum in horizontal position. For low steps and low collision velocities, the ball behavior resembles the simulation result where the pendulum is directed downwards. In contrast, with high steps and high impact velocities, the test results approach the simulation model with the pendulum in horizontal position. For GimBall, the benefit from the elevated pendulum can be as much as 1-cm increase in the maximum step height.

Fig. 6 shows also the theoretical maximum step height based on conservation of energy as well as the maximum step height calculated with the quasi-static torque balance. In case of the GimBall, the energy-based estimation appears to be useful until 2-3 cm step height, respective with 0.6-0.7 m/s impact velocity. Above that, it may be anticipated that significant amount of energy is lost in inelastic collision. In addition, the collision geometry may re-direct the kinetic energy in such a way that doesn't aid in overcoming the obstacle, i.e. at least partially backwards. Further, the moving pendulum inside the ball may also adopt some of the kinetic energy and redistribute it in a manner that doesn't help ball progression.

Traditional quasi-static model neglects the momentum and energy of the moving robot. As may be seen from Fig. 6, the quasi-static model underestimates severely the performance of a moving spherical robot.

Fig. 7 shows on the top row the RC-controlled GimBall passing over a small 21-mm step with a low velocity (0.76 m/s). The ball has reached the target velocity well before the collision and the pendulum remains pointing downwards during the impact. The middle row shows a larger 31-mm step with almost the same velocity (0.78 m/s). The pendulum clearly elevates during the impact which aids in passing over the step. The third row presents a tall 56-mm step and high velocity (1.09 m/s). Due to limited 120-cm acceleration distance, the ball accelerates until the impact and holds the pendulum almost in a horizontal position until the step has been passed. The two simulation models in Fig. 6 thus relate to the three test results in Fig. 7; showing the pendulum pointing downwards, a horizontal pendulum, and a transition between those. Fig. 8 demonstrates the comparable

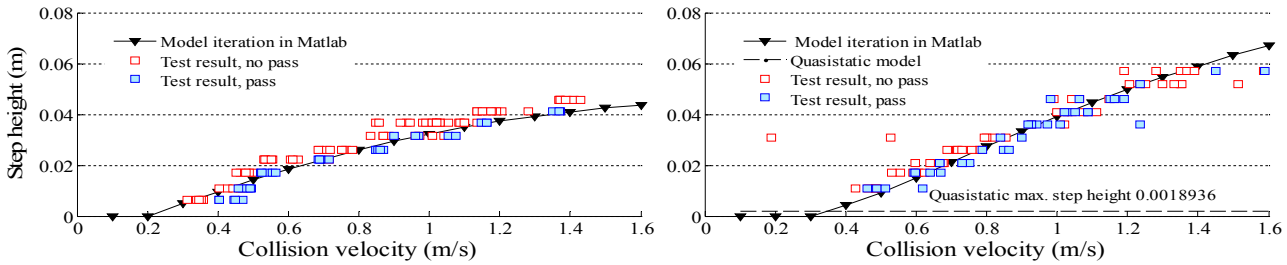

Fig. 5. Free-rolling simulation results from the dynamic model in Matlab, experimental results, and the quasi-static model. Left: ShellBall step overcoming capability as a function of collision velocity. Right: GimBall step overcoming capability

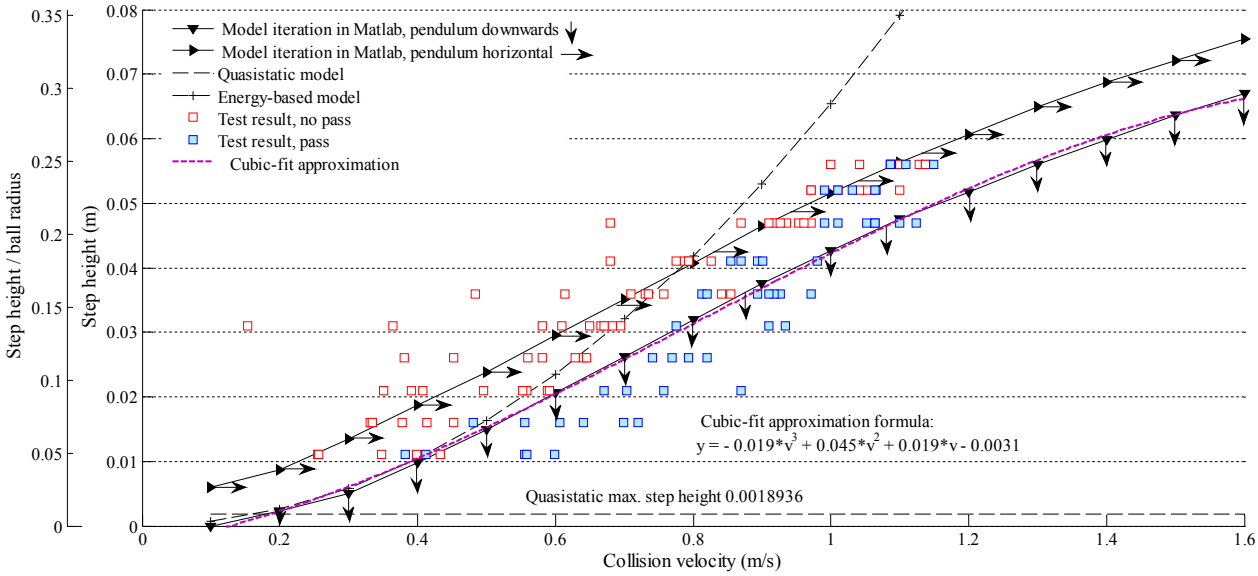

Fig. 6. Gimball step crossing performance under manual velocity control, compared to the simulated results with pendulum pointing downwards and with pendulum in horizontal position

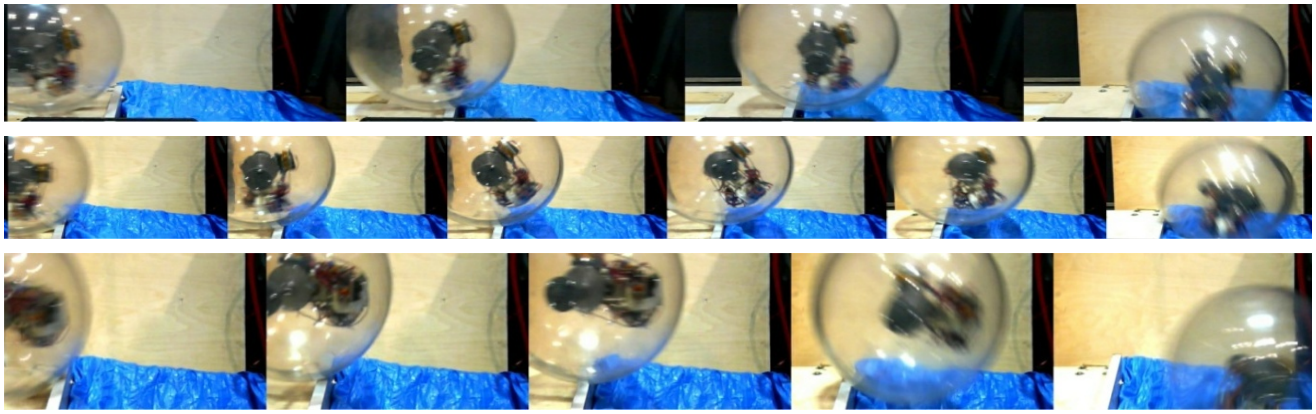

Fig. 7. GimBall crossing a step under manual control. Top: Small step, low velocity, pendulum downwards also during crossing. Middle: Higher step, low velocity, pendulum rises during impact. Below: High step, high velocity, pendulum elevated already before collision, maintains this position

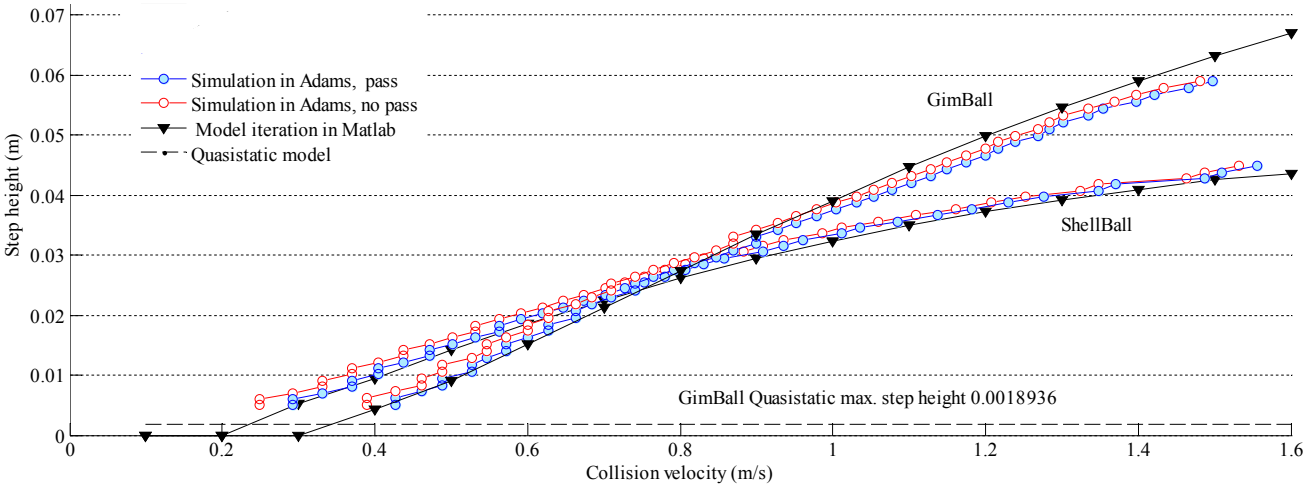

Fig. 8. GimBall and ShellBall free-rolling step overcoming capability as a function of collision velocity. Simulation results from the dynamic model in Matlab compared with the results from simulation in Adams

simulation results of the dynamic model in Matlab and the simulations in Adams.

The control algorithms described in Section 4.2 were applied for the pendulum control in simulations only. In the practical tests, the pendulum was either completely free (detached from the motor) or driven manually with a RC-equipment and visual feedback.

8 Model application in practice

Together with the ascending bracketing method, the simulation model can be applied off-line for ball-robot mobility analysis as well as for path planning.

For on-line path-planning and decision making, a faster approach is necessary. For this purpose, it is possible to approximate the simulated step-height vs. collision-velocity curve with a pre-calculated 3rd degree polynomial curve, shown also in Fig. 6. With the help of the polynomial, the robot can quickly deduce whether to try to overcome the detected obstacle and at which velocity, or whether to find another way around.

9 Conclusions

Many usual every-day features; for example door steps, carpets, electric cords, and scattered toys; create possible obstacles for the robot mobility in home-environment. We have introduced an extended decoupled ball-robot model and applied it to predict the step-overcoming capability of the robot. The results have been confirmed with practical experiments using two very different platforms: a ball-robot with a pendulum, and a simple ball shell without any mechanisms. The model works well in both cases.

To predict step over-coming capability, prior work has presented quasi-static models as well as energy-based models. In a dynamic collision, our model based on

contact forces and ball dynamics outperforms them both. In addition to these three approaches, also models based on preservation of momentum have been applied for Tumbleweed-rovers. However, Tumbleweeds do not posses any internal mechanisms that may participate in the collision event. In contrast, our model includes also the internal driving pendulum and the actuation of it.

With the aid of ascending bracketing method, our model can be used to derive the maximum traversable step height for the given collision velocity. This approach is applicable for off-line analysis of ball-robot designs as well as for off-line path planning. For on-line analyses, it is possible to approximate the simulated step-height vs. collision-velocity curve with a 3rd degree polynomial.

Environmental constraints such as the available acceleration distance have an effect on practical step overcoming capability and path planning. The 120-cm acceleration distance used in the experiments reflects well a situation where the ball needs to enter from a narrow hallway into a room over a door-step. Even if there was plenty of room for speeding up, in certain cases it can be beneficial to apply 'last minute' acceleration that sets the pendulum into desired orientation for the moment of collision.

If compared to the quasi-static model, the significantly increased dynamic step over-coming capability gives more freedom in mechanical design of the robot: In a dynamic case, it is not as essential to maximize the pendulum length or the amount of mass placed in the end of the pendulum.

Further work includes application and demonstration of the results in path-planning and decision-making simulations and experiments. In addition, the applicability of the momentum-based collision model deserves some further attention.

References

[1] T. Ylikorpi & J. Suomela, Ball-shaped Robots, *Climbing & Walking Robots, Towards New Applications* (Vienna: InTech, 2007), 235-256.

[2] J. Suomela & T. Ylikorpi, Ball-shaped robots: An historical overview and recent developments at TKK, *Springer Tracts in Advanced Robotics, Field and Service Robotics, 25*, 2006, 343-354.

[3] A. Koshiyama & K. Yamafuji, Design and control of an all-direction steering type mobile robot, *International Journal of Robotics Research, 12*(5), 1993, 411-419.

[4] A. Halme, T. Schönberg & Y. Wang, Motion control of a spherical mobile robot, *Proc. IEEE International Workshop on Advanced Motion Control*, Mie, Japan, 1996, 259-264.

[5] F. Michaud & S. Caron, Roball, the rolling robot, *Autonomous Robots, 12*(2), 2002, 211-222.

[6] *Sphero* [Online] http://www.gosphero.com/ (Accessed: 12/5, 2013).

[7] *GuardBOT* [Online] http://www.guardbot.org/ (Accessed: 12/5, 2013).

[8] S. Spitzmüller, *Microcontroller based control system for a rolling minirobot,* Master's Thesis, Department of Automation and Systems Technology, Helsinki University of Technology, 1998.

[9] M. Nagai, *Control System of a Ball-shaped Robot,* Master's Thesis, Department of Automation and Systems Technology, Helsinki University of Technology, 2008.

[10] J.F. Laplante, *Étude de la dynamique d'un robot sphérique et de son effet sur l'attention et la mobilité de jeunes enfants,* (in French), Master's Thesis, Université De Sherbrooke, Faculté de genie, Département de génie mécanique, 2004.

[11] F.C. Bruhn, K. Pauly & V. Kaznov, Extremely low mass spherical rovers for extreme environments and planetary exploration enabled with MEMS, *European Space Agency, (Special Publication) ESA SP 603,* 2005, 347-354.

[12] J.C. Yoon, S.S. Ahn & Y.J. Lee, Spherical robot with new type of two-pendulum driving mechanism, *Proc. International Conference on Intelligent Engineering Systems*, Poprad, Slovakia, 2011, 275-279.

[13] W. Zhuang, X. Liu, C. Fang & H. Sun, Dynamic modeling of a spherical robot with arms by using Kane's method, *Proc. 4th International Conference on Natural Computation*, Jinan, 2008, 373-377.

[14] Q. Jia, H. Sun & D. Liu, Analysis of Actuation for a Spherical Robot, *Proc. IEEE Conference on Robotics, Automation and Mechatronics*, Chengdu, China, 2008, 266-271.

[15] T. Yu, H. Sun & Y. Zhang, Dynamic analysis of a spherical mobile robot in rough terrains, *Proc. SPIE 8044, Sensors and Systems for Space Applications IV, 80440V*, Orlando, 2011.

[16] D. Liu, H. Sun & Q. Jia, Stabilization and path following of a spherical robot, *Proc. IEEE International Conference on Robotics, Automation and Mechatronics*, Chengdu, 2008, 676-682.

[17] M. Zheng, Q. Zhan, J. Liu & Y. Cai, Control of a Spherical Robot: Path Following Based on Nonholonomic Kinematics and Dynamics, *Chinese Journal of Aeronautics, 24*(3), 2011, 337-345.

[18] Q. Jia, Y. Zheng, H. Sun, H. Cao & H. Li, Motion control of a novel spherical robot equipped with a flywheel, *Proc. IEEE International Conference on Information and Automation*, Zhuhai, Macau, 2009, 893-898.

[19] M. Yue, Z. Deng, X. Yu & W. Yu, Introducing HIT Spherical Robot: Dynamic Modeling and Analysis Based on Decoupled Subsystem, *Proc. IEEE International Conference on Robotics and Biomimetics*, Kunming, China, 2006, 181-186.

[20] J. Kim, H. Kwon & J. Lee, A rolling robot: Design and implementation, *Proc. 7th Asian Control Conference*, Hong Kong, 2009, 1474-1479.

[21] E. Kayacan, Z.Y. Bayraktaroglu & W. Saeys, Modeling and control of a spherical rolling robot: a decoupled dynamics approach, *Robotica, 30*(4), 2012, 671-680.

[22] Y. Cai, Q. Zhan & X. Xi, Neural Network Control for the Linear Motion of a Spherical Mobile Robot, *International Journal of Advanced Robotic Systems, 8*(4), 2011, 79-87.

[23] S. Mahboubi, M.M. Seyyed Fakhrabadi & A. Ghanbari, Design and implementation of a novel spherical mobile

robot, *Journal of Intelligent and Robotic Systems: Theory and Applications, 71*(1), 2013, 43-64.

[24] Q. Zhang, Q. Jia, H. Sun & Z. Gong, Application of a Genetic Algorithm-Based PI Controller in a Spherical Robot, *Proc. IEEE International Conference on Control and Automation*, Christchurch, 2009, 180-184.

[25] D. Liu, H. Sun & Q. Jia, A Family of Spherical Mobile Robot: Driving Ahead Motion Control by Feedback Linearization, *Proc. 2nd International Symposium on Systems and Control in Aerospace and Astronautics*, Shenzhen, 2009, 1-6.

[26] M. Kamaldar, M.J. Mahjoob, M. Haeri Yazdi, H. Vahid-Alizadeh & S. Ahmadizadeh, A control synthesis for reducing lateral oscillations of a spherical robot, *Proc. IEEE International Conference on Mechatronics*, Istanbul, 2011, 546-551.

[27] T. Yu, H. Sun, Y. Zhang & W. Zhao, Control and stabilization of a pendulum-driven spherical mobile robot on an inclined plane, *Proc. 11th International Symposium on Artificial Intelligence, Robotics and Automation in Space* , Turin, Italy, 2012.

[28] M. Yue & B. Liu, Adaptive control of an underactuated spherical robot with a dynamic stable equilibrium point using hierarchical sliding mode approach, *International Journal of Adaptive Control and Signal Processing,* 2013.

[29] T. Ylikorpi, P. Forsman, A. Halme & J. Saarinen, Unified representation of decoupled dynamic models for pendulum-driven ball-shaped robots, paper submitted to be published in *Proc. 28th European Conference on Modelling and Simulation*, Brescia, Italy, 2014.

[30] W. Zhao, H. Sun, Q. Jia & Y. Zhang, Mechanical analysis about the spherical mobile robot on the moon environment, *Proc. SPIE Int Soc Opt Eng,* 8044, 2011.

[31] J. Antol, P. Calhoun, J. Flick, G. Hajos, R. Kolancinski, D. Minton, R. Owens & J. Parker, *Low Cost Mars Surface Exploration: The Mars Tumbleweed.* NASA TM-2003-212411, 2003.

[32] R.M. Kolacinski & R.D. Quinn, *Design of a Biologically Inspired Martian Rover based upon the Russian Thistle (Salsola tragus),* 2004. Available at: http://naca.central.cranfield.ac.uk/dcsss/2004/B31_Design_Mars_Rover_V_EDITfinal.pdf

[33] J.J. Flick & M.D. Toniolo, Preliminary dynamic feasibility and analysis of a spherical, wind-driven (tumbleweed), Martian Rover, *43rd AIAA Aerospace Sciences Meeting and Exhibit - Meeting Papers,* 2005, 11901.

[34] A.E. Hartl, *Modeling and Simulation of the Dynamics of Dissipative, Inelastic Spheres with Applications to Planetary Rovers and Gravitational Billiards*, Ph.D. dissertation, North Carolina State University, Aerospace Engineering, 2011.

[35] T.R. Kane & D.A. Levinson, *Dynamics: Theory and Applications* (New York: McGraw-Hill, 1985).

[36] T. Li, Design and Analysis of a Wind-Driven Spherical Robot with Multiple Shapes for Environment Exploration, *J.Aerospace Eng., 24*(1), 2011, 135-139.

[37] Y.S. Liang, X.L. Zhang, H. Hao, Y.F. Yang, W.T. Jin & Z. Sang, A deformable spherical planet exploration robot, *Proc. International Conference on Graphic and Image Processing*, Singapore, 2013.

[38] H. Goldstein, C. Poole & J. Safko, *Classical mechanics* 3rd ed. (San Francisco, CA: Addison-Wesley, 2002).

[39] K.R. Symon, *Mechanics* 2nd ed. (Reading, MA: Addison-Wesley, 1960).

[40] *Modeling Impact.* Tech Articles ID KB8013895, 1987. Available at: http://simcompanion.mscsoftware.com/infocenter/

[41] *Contrasting the restitution and impact methods in v11.0 contact.* Tech Articles ID KB8014800, 2009. Available at: http://simcompanion.mscsoftware.com/infocenter/

[42] *Adams/Solver help - Adams 2013.* Docs ID DOC10407, solver_2013.pdf. Available at: http://simcompanion.mscsoftware.com/infocenter/

[43] *Adams/View help - Adams 2013.* Docs ID DOC10410, view_2013.pdf, 2013. Available at: http://simcompanion.mscsoftware.com/infocenter/

[44] P. Flores, J. Ambrósio, J.C. Claro & H.M. Lankarani, Influence of the contact-impact force model on the dynamic response of multi-body systems, *Proceedings of the Institution of Mechanical Engineers, Part K: Journal of Multi-Body Dynamics, 220*(1), 2006, 21-34.

[45] D.E. Stewart, Rigid-body dynamics with friction and impact, *SIAM Review, 42*(1), 2000, 3-39.